Yan and Zhang *Earth, Planets and Space* (2022) 74:47
https://doi.org/10.1186/s40623-022-01602-9

Earth, Planets and Space

FULL PAPER Open Access

Assessment of the performance of GPS/Galileo PPP-RTK convergence using ionospheric corrections from networks with different scales

Zhongbao Yan and Xiaohong Zhang*

Abstract

The rapid convergence of precise point positioning real-time kinematics (PPP-RTK) with centimeter-level accuracy is of utmost importance for many applications. One way of accelerating this convergence is to explore the use of ionospheric models and multiple global navigation satellite system (GNSS) observations, e.g., Global Positioning System (GPS) and Galileo Satellite Navigation System (Galileo) observations. Because the temporal and spatial variations of the ionosphere are significant, convergence analysis of PPP-RTK should be investigated in networks with different scales, especially networks with large differences in their scales. This study describes the convergence performance of PPP-RTK using GPS/Galileo observations derived from networks with different scales under medium ionospheric conditions. Slant ionospheric corrections were first estimated from the reference network and then imported as virtual observations to enhance the convergence performance of PPP-RTK at the user interface. The results show that for the 165-km reference site spacing, the portions of single-differenced (SD) ionospheric residuals within 0.3 total electron content units (TECU) were 85.2% and 81.7% for the GPS and Galileo observations, respectively. Considering the 90th percentile of horizontal position errors, the PPP-RTK convergence time within the network with 165-km spacing was shortened from 2.5 min for GPS-only observations to 2.0 min for integrated GPS + Galileo observations. For the network of about 50 km, the proportions of the SD ionospheric residuals of the GPS and Galileo constellation within 0.3 TECU were 95.9% and 82.8%, respectively. The PPP-RTK convergence time of the 90th percentile horizontal positioning errors based on GPS-only observations was 2.0 min but 1.5 min based on integrated GPS + Galileo observations. Using GPS and Galileo observations, the convergence time could be reduced by 25% for the network with 50-km spacing. Our results suggest that the convergence time of PPP-RTK depends on the scale of the reference network and becomes shorter as the scale of the network decreases. Compared with the GPS-only PPP-RTK, the GPS/Galileo PPP-RTK could shorten the convergence time further.

Keywords: PPP-RTK, GNSS, Slant ionospheric corrections, Total electron content unit

*Correspondence: xhzhang@sgg.whu.edu.cn
School of Geodesy and Geomatics, Wuhan University, 129 Luoyu Road, Wuhan 430079, China

Graphical Abstract

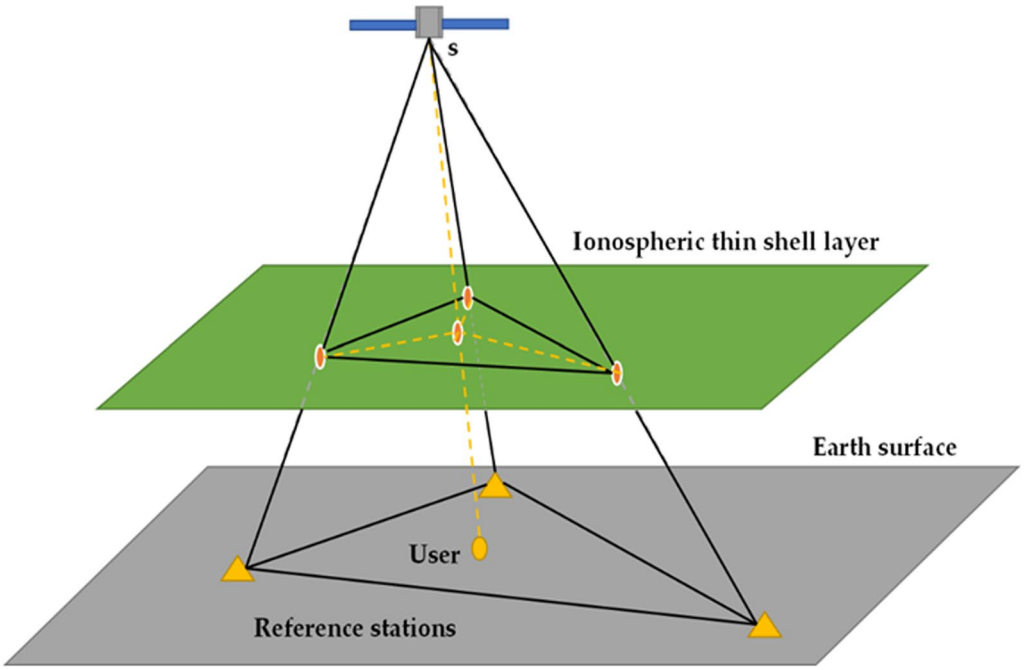

Introduction

In the past few years, precise point positioning (PPP) has become a widely applied method for providing precise positioning due to its convenience and efficiency (Zumberge et al. 1997; Kouba and Heroux 2011). Unfortunately, the convergence time of conventional PPP is still half an hour or longer. To reduce the convergence time and improve positioning accuracy, several PPP ambiguity resolution (AR) approaches have been proposed in the past few years to restore the integer feature of ambiguities (Ge et al. 2008; Collins 2008; Laurichesse et al. 2009; Mervart et al. 2008; Bertiger et al. 2010; Teunissen et al. 2010; Geng et al. 2012; Loyer et al. 2012). The relationship between these methods has also been demonstrated (Geng et al. 2010a; Shi and Gao 2014; Teunissen and Khodabandeh 2015). However, fast and reliable ambiguity resolution is still not available due to the obstacle of atmospheric errors, especially ionospheric delays. In such cases, a novel technology called PPP real-time kinematic (PPP-RTK) has been proposed (Wubbena et al. 2005; Teunissen et al. 2010; Mervart et al. 2008; Geng et al. 2011). PPP-RTK utilizes the precise atmospheric corrections generated from the reference network to accelerate the ambiguity resolution. Moreover, the PPP-RTK technique also has the advantage of low bandwidth requirements and one-way communication, thus providing a promising opportunity for the emerging mass market and automotive applications.

Benefiting from the unique advantages of PPP-RTK, great efforts in recent years have been focused on PPP-RTK with promising results, both in research as well as in applications (Li et al. 2011, 2020; Zhang et al. 2011; Odijk and Zhang 2012; Psychas and Verhagen 2020; Nadarajah et al. 2018; Ma et al. 2020). Li et al. (2011) implemented a regional augmentation PPP experiment in a network with an average distance of about 60 km. The results showed that an almost instantaneous ambiguity resolution of global positioning system (GPS) PPP was available if the interpolated atmospheric corrections derived from the reference stations could be obtained. Zhang et al. (2011) tested two GPS CORS networks with an average distance ranging from 60 to 100 km. The results demonstrated the performance of ambiguity fixing and positioning accuracy have achieved ideal effects. Odijk and Zhang (2012) performed the single-frequency PPP-RTK using a geodetic receiver as well as a low-cost receiver. The results showed that the cm-level positioning accuracy can be obtained by utilizing the atmospheric corrections of the reference networks and observations of less than 10 min. Psychas and Verhagen (2020) demonstrated that sub-decimeter horizontal positioning accuracy could be achieved almost instantaneously for a network with 68-km spacing. However, when

the inter-station distance is increased to 237 km, it required about 7.0 min to achieve a sub-decimeter horizontal positioning accuracy when only GPS observations were used. Currently, the rapid development of multi-constellation global navigation satellite systems (GNSS) has created new opportunities for PPP-RTK. Li et al. (2020) investigated the performance of GPS/BeiDou Navigation Satellite System (GPS/BDS) PPP-RTK. The results revealed that PPP-RTK fixed solutions could be achieved in an average of 1.5, 1.6, and 1.2 epochs, and the corresponding positioning root-mean-square (RMS) in the east, north, and vertical components was 0.80, 0.47, and 1.97 cm for GPS alone; 0.98, 0.73, and 2.97 cm for BDS alone; and 0.56, 0.35, and 2.33 cm for integrated GPS+BDS observations. Nadarajah et al. (2018) used the GPS, BDS, and Galileo Satellite Navigation System (Galileo) observations to investigate the positioning and convergence performance of PPP-RTK scenarios. The results indicated that with a regional network of about 30 km, sub-decimeter positioning accuracy in the horizontal and vertical components could be achieved within 4.5 and 5.0 min for GPS alone and 1.0 and 0.5 min for integrated multi-GNSS (GPS, BDS, and Galileo) observations. Ma et al. (2020) investigated multi-GNSS PPP-RTK in the local area. Their results showed that the multi-GNSS observations could accelerate the ambiguity resolution of PPP for GPS alone. Unfortunately, they investigated the positioning and convergence performance without utilizing ionospheric corrections.

Despite much work having been devoted to investigating the impact of ionospheric corrections for PPP-RTK performance (e.g., multi-GNSS PPP-RTK and multi-scale PPP-RTK), there are still some potential problems that need to be further researched and clarified. For instance, Psychas and Verhagen (2020) investigated regional augmented PPP AR by utilizing ionospheric corrections derived from networks with different scales. However, only GPS observations were used to generate the ionospheric delays and to investigate the positioning and convergence performance of PPP-RTK. Thus, they did not explore the impact of multi-GNSS observations on PPP-RTK performance and the accuracy of ionospheric delays in networks with different scales. Although multi-scale PPP-RTK using multi-GNSS observations was also investigated, Nadarajah et al. (2018) only demonstrated regional augmented PPP AR in small-scale reference networks and did not explore the regional augmented PPP AR for networks with large differences in scale.

As indicated by previous studies, the ionospheric delays derived from the regional GNSS network play an important role in PPP-RTK for accelerating ambiguity resolution. However, the spatial resolution and accuracy of the generated ionospheric corrections are associated with the scale of the reference network and the stations' distribution in a network. This may affect its performance in PPP-RTK when adopted as an accurate prior constraint. Furthermore, current research concerning multi-GNSS PPP-RTK has mostly used small-scale networks, with the aim of investigating the convergence and positioning performance. The performance of multi-GNSS PPP-RTK with ionospheric corrections derived from networks with large differences in their scales still needs further investigation. For this reason, this study aimed to systematically analyze the convergence performance of PPP-RTK using the ionospheric corrections of GPS and the Galileo constellation derived from networks with large differences in their scales.

The remainder of this study is organized as follows. "Methods" section introduces the uncombined PPP (UCPPP) AR algorithm and then describes the estimation, representation, and constraint methods of ionospheric correction. The design of the PPP-RTK platform software system is also presented in this part as well. "Results" section outlined the strategies used for data processing and focuses on the assessment of the convergence performance of PPP-RTK utilizing GPS/Galileo observations from two networks with different scales. In "Discussion" section, some conclusions and perspectives are provided.

Methods

In this section, the mathematical models for undifferenced and uncombined PPP-RTK are summarized first, followed by an investigation of the methods that can generate and interpolate slant ionospheric delays; next, the augmented PPP model is discussed. The comprehensive data processing strategies are also presented as well.

UCPPP observation equations

The original observation equations for the dual-frequency pseudo-range and carrier phase observations are given as:

$$\begin{cases} P_1 = \rho + c\mathrm{dt}^{\mathrm{r}} - c\mathrm{dt}^{\mathrm{s}} + T + I_1 + D^{\mathrm{r}}_{P_1} - D^{\mathrm{s}}_{P_1} + \varepsilon_{P_1} \\ P_2 = \rho + c\mathrm{dt}^{\mathrm{r}} - c\mathrm{dt}^{\mathrm{s}} + T + \gamma_2 I_1 + D^{\mathrm{r}}_{P_2} - D^{\mathrm{s}}_{P_2} + \varepsilon_{P_2} \\ L_1 = \rho + c\mathrm{dt}^{\mathrm{r}} - c\mathrm{dt}^{\mathrm{s}} + T - I_1 + \lambda_1(N_1 + B^{\mathrm{r}}_{L_1} - B^{\mathrm{s}}_{L_1}) + \varepsilon_{L_1} \\ L_2 = \rho + c\mathrm{dt}^{\mathrm{r}} - c\mathrm{dt}^{\mathrm{s}} + T - \gamma_2 I_1 + \lambda_2(N_2 + B^{\mathrm{r}}_{L_2} - B^{\mathrm{s}}_{L_2}) + \varepsilon_{L_2} \end{cases}, \quad (1)$$

where P_1 and P_2 denote the pseudo-range measurements and L_1 and L_2 are carrier phase measurements on the two frequencies which are actually L_1, L_2 for GPS, and E1, E5a for Galileo; ρ is the distance between the antenna phase center of both the satellite and receiver corrected for many errors, including phase wind-up, Shapiro signal propagation delay, solid and ocean tides, pole tides, relativistic effect, antenna phase center offsets (PCOs), and phase center variations (PCVs) for the satellite and receiver; dt^{r} and dt^{s} are the clock offsets of the satellite and receiver, respectively; c is the speed of light in a vacuum; T is the total troposphere delay (m); I_1 represents the slant ionospheric delay at frequency L_1 (m); N_1 and N_2 are the ambiguity parameters at frequency ($k=1, 2$); λ_k denotes the wavelength at frequency k ($k=1, 2$); ε_{P_k} and ε_{L_k} are the measurement noise and multipath effect for the pseudo-range and carrier phase measurements at frequency k ($k=1, 2$), respectively; $D^{\mathrm{r}}_{P_k}$ and $D^{\mathrm{s}}_{P_k}$ are the pseudo-range hardware delay of the receiver and satellite at frequency k ($k=1, 2$), respectively; $B^{\mathrm{r}}_{L_k}$ and $B^{\mathrm{s}}_{L_k}$ are the carrier phase hardware delay of the receiver and satellite at frequency k ($k=1, 2$), respectively; and $\gamma_2 = \frac{f_1^2}{f_2^2}$, where f_k denotes the frequency k ($k=1, 2$).

If we consider the ionospheric free (IF) satellite clocks, the UCPPP model can be reparametrized as (Laurichesse and Privat 2015; Xiang et al. 2020):

$$\begin{cases} P_1 = \rho + c\left(\mathrm{dt}^{\mathrm{r}} + D^{\mathrm{r}}_{P_{\mathrm{IF}}}\right) - c\left(\mathrm{dt}^{\mathrm{s}} + D^{\mathrm{s}}_{P_{\mathrm{IF}}}\right) + T + \left(I_1 - \frac{f_2^2}{f_1^2 - f_2^2}\left(\mathrm{DCB}^{\mathrm{r}}_{P_1-P_2} - \mathrm{DCB}^{\mathrm{s}}_{P_1-P_2}\right)\right) + \varepsilon_{P_1} \\ P_2 = \rho + c\left(\mathrm{dt}^{\mathrm{r}} + D^{\mathrm{r}}_{P_{\mathrm{IF}}}\right) - c\left(\mathrm{dt}^{\mathrm{s}} + D^{\mathrm{s}}_{P_{\mathrm{IF}}}\right) + T + \gamma_2\left(I_1 - \frac{f_2^2}{f_1^2 - f_2^2}\left(\mathrm{DCB}^{\mathrm{r}}_{P_1-P_2} - \mathrm{DCB}^{\mathrm{s}}_{P_1-P_2}\right)\right) + \varepsilon_{P_2} \\ L_1 = \rho + c\left(\mathrm{dt}^{\mathrm{r}} + D^{\mathrm{r}}_{P_{\mathrm{IF}}}\right) - c\left(\mathrm{dt}^{\mathrm{s}} + D^{\mathrm{s}}_{P_{\mathrm{IF}}}\right) + T - \left(I_1 - \frac{f_2^2}{f_1^2 - f_2^2}\left(\mathrm{DCB}^{\mathrm{r}}_{P_1-P_2} - \mathrm{DCB}^{\mathrm{s}}_{P_1-P_2}\right)\right) + \lambda_1\tilde{N}_1 + \varepsilon_{L_1} \\ L_2 = \rho + c\left(\mathrm{dt}^{\mathrm{r}} + D^{\mathrm{r}}_{P_{\mathrm{IF}}}\right) - c\left(\mathrm{dt}^{\mathrm{s}} + D^{\mathrm{s}}_{P_{\mathrm{IF}}}\right) + T - \gamma_2\left(I_1 - \frac{f_2^2}{f_1^2 - f_2^2}\left(\mathrm{DCB}^{\mathrm{r}}_{P_1-P_2} - \mathrm{DCB}^{\mathrm{s}}_{P_1-P_2}\right)\right) + \lambda_2(\tilde{N}_1 + \tilde{N}_{\mathrm{W}}) + \varepsilon_{L_2} \end{cases}, \tag{2}$$

where $D^{\mathrm{r}}_{P_{\mathrm{IF}}}$ and $D^{\mathrm{s}}_{P_{\mathrm{IF}}}$ represent the pseudo-range hardware delay based on the ionospheric free combination for the receiver and satellite, respectively; $\mathrm{DCB}^{\mathrm{r}}_{P_1-P_2}$ and $\mathrm{DCB}^{\mathrm{s}}_{P_1-P_2}$ represent the P_1/P_2 signals differential code biases (DCBs) of the receiver and satellite, respectively; $\tilde{N}_1 = N_1 + B^{\mathrm{r}}_{L_1} - B^{\mathrm{s}}_{L_1} - \left(c(D^{\mathrm{r}}_{P_{\mathrm{IF}}} - D^{\mathrm{s}}_{P_{\mathrm{IF}}}) + \frac{f_2^2}{f_1^2 - f_2^2}\left(\mathrm{DCB}^{\mathrm{r}}_{P_1-P_2} - \mathrm{DCB}^{\mathrm{s}}_{P_1-P_2}\right)\right)\Big/\lambda_1$ is the floating narrow-lane (NL) ambiguity (cycles) containing the biases of both the carrier phase and the pseudo-range; $\tilde{N}_2 = N_2 + B^{\mathrm{r}}_{L_2} - B^{\mathrm{s}}_{L_2} - \left(c(D^{\mathrm{r}}_{P_{\mathrm{IF}}} - D^{\mathrm{s}}_{P_{\mathrm{IF}}}) + \frac{f_1^2}{f_1^2 - f_2^2}\left(\mathrm{DCB}^{\mathrm{r}}_{P_1-P_2} - \mathrm{DCB}^{\mathrm{s}}_{P_1-P_2}\right)\right)\Big/\lambda_2$ is the floating ambiguity at a frequency of 2 (cycles) containing the biases of both the carrier phase and the pseudo-range; and $\tilde{N}_{\mathrm{W}} = \tilde{N}_2 - \tilde{N}_1$ is the floating wide-lane (WL) ambiguity (cycles) containing the biases of both the carrier phase and the pseudo-range.

If known satellite clock corrections and DCBs are used to correct the observation equations of the UCPPP model, the corresponding simplified formulae read:

$$\begin{cases} P_1 = \rho + c\widetilde{\mathrm{dt}}^{\mathrm{r}} + T + \tilde{I}_1 + \varepsilon_{P_1} \\ P_2 = \rho + c\widetilde{\mathrm{dt}}^{\mathrm{r}} + T + \gamma_2\tilde{I}_1 + \varepsilon_{P_2} \\ L_1 = \rho + c\widetilde{\mathrm{dt}}^{\mathrm{r}} + T - \tilde{I}_1 + \lambda_1\tilde{N}_1 + \varepsilon_{L_1} \\ L_2 = \rho + c\widetilde{\mathrm{dt}}^{\mathrm{r}} + T - \gamma_2\tilde{I}_1 + \lambda_2(\tilde{N}_1 + \tilde{N}_{\mathrm{W}}) + \varepsilon_{L_2} \end{cases}, \tag{3}$$

where $\widetilde{\mathrm{dt}}^{\mathrm{r}} = \mathrm{dt}^{\mathrm{r}} + D^{\mathrm{r}}_{P_{\mathrm{IF}}}; \tilde{I}_1 = I_1 - \frac{f_2^2}{f_1^2 - f_2^2}\mathrm{DCB}^{\mathrm{r}}_{P_1-P_2}$.

If the UCPPP model can be corrected by utilizing the satellite DCBs, and if external ionospheric products are not available, the ionospheric delays contaminated by the receiver's DCBs will be considered as an unknown parameter to be estimated. This way, the state vector of unknowns is $\vec{X} = \left[x\ y\ z\ \widetilde{\mathrm{dt}}^{\mathrm{r}}\ T\ \tilde{I}_1\ \tilde{N}_1\ \tilde{N}_{\mathrm{W}}\right]^{\mathrm{T}}$, which will be estimated by the UCPPP model using a Kalman filter approach. The slant ionospheric corrections can be generated only when the WL and NL ambiguity can be fixed successfully.

The observation equations of the UCPPP model above can be applied to the entire PPP-RTK network and the user components. Additionally, for the network component, the station coordinates should be fixed to the true values to accelerate the convergence for the estimated parameters in the PPP filter. However, the user's receiver positions have to be estimated to evaluate the convergence performance in the user components.

UCPPP AR

Since satellites' pseudo-range and carrier phase bias products have been made available by GNSS analysis centers, satellites' pseudo-range biases can be corrected by DCBs or observable specific signal biases (OSBs), and

carrier phase biases can be corrected by uncalibrated phase delays (UPDs) or OSBs (Banville et al. 2020; Liu et al. 2021). According to Eq. (3), the pseudo-range and carrier phase biases from receivers are mainly absorbed by ambiguities, slant ionospheric delays, and receiver clock offsets. Thus, the satellite-dependent biases could be removed in advance; instead, single-difference (SD) ambiguities between satellites had to be formed to remove the biases of the receiver components. Specifically, we have chosen the satellite with the highest elevation as the reference satellite and found the single difference between the reference satellite and other satellites in the same satellite system (Li et al. 2016).

The PPP AR algorithm is divided into two key steps. Firstly, the SD WL ambiguities can be resolved by rounding. The equation for calculating the probability P_0 of fixing SD WL ambiguity is given as (Dong and Bock 1989):

$$\begin{cases} P_0 = 1 - \sum_{i=1}^{\infty} \left[\mathrm{erfc}\left(\frac{i-(B-n)}{\sqrt{2}\delta} \right) - \mathrm{erfc}\left(\frac{i+(B-n)}{\sqrt{2}\delta} \right) \right] \\ \mathrm{erfc}(x) = \frac{2}{\sqrt{\pi}} \int_x^{\infty} e^{-t^2} \mathrm{dt} \end{cases}, \tag{4}$$

where P_0 represents the probability of fixing SD WL ambiguity; B and δ represents the floating SD WL ambiguity and its accuracy, respectively; and n denotes the nearest integer of B.

The fixed SD WL ambiguities are then considered as virtual observations to update the remaining unknowns and variance–covariance matrix to enhance the fixing of SD NL ambiguities. The optimal integer solution for SD NL ambiguities can be found by applying the least-square ambiguity decorrelation adjustment (LAMBDA) method (Teunissen 1995). Since the residual model errors can affect the fractional part of SD NL ambiguities, ambiguity validation is particularly important to fix SD NL ambiguities reliably (Ge et al. 2008; Cui et al. 2021). Specifically, for ambiguity validation, the ratio and bootstrapping success rate are frequently utilized for AR (Ji et al. 2010; Verhagen 2005, 2003; Li and Zhang 2015). The bootstrapping success rate can be applied here. It has been regarded as a lower bound for the integer least-squares (ILS) success rate (Teunissen 1998; Blewitt 1989). However, the computed success rate always cannot objectively reflect the real success rate of actual observations although the computed success rate could still be high (Li and Zhang 2015). Meanwhile, the threshold of ratio is only determined by the simulated measurements at present, so the empirical value cannot be efficiently applied to validate the ambiguity resolution (Blewitt 1989). Furthermore, when the data are initialized or the satellite elevation is too low, it is difficult to accurately fix ambiguities due to the low accuracy. Therefore, it is essential to apply strict quality control strategies for the determination of the ambiguity subset, which is a special case of integer-aperture estimation (Teunissen 2005).

The detailed quality control parameters of UCPPP AR used in this study are listed in Table 1.

Figure 1 shows the flowchart of the UCPPP AR algorithm. First, the subset of SD WL ambiguities was determined carefully. Next, the SD WL ambiguities were first fixed by the rounding method in a one-step approach and applied as a constraint to update the normal equations of the UCPPP model. Afterwards, the LAMBDA algorithm was applied to fix the subset of SD NL ambiguities in a two-step approach. In particular, we require at least four resolved ambiguities for partial ambiguity fixing. If the number of ambiguities was less than four or if partial ambiguity fixing could pass the threshold of either the one-step or two-step approach, we kept the floating solutions instead and moved on to the next epoch.

Estimation, representation, and constraint of ionospheric corrections

To provide precise ionospheric corrections for users, proper derivation and representation of ionospheric corrections play a critical role in the positioning performance of PPP-RTK. In our study, the precise slant ionospheric delays were derived from the UCPPP model with a fixed ambiguity method. In fact, because of the impact of UPDs, the un-difference (UD) ambiguity and SD ambiguity are no longer integers (Blewitt 1989). The removal of UPDs from both satellite and receiver is essential for PPP-AR to recover the ambiguity's integer property. Proceeding this way, when satellite-dependent UPDs can be corrected by applying OSBs/UPDs products, and receiver-dependent UPDs can be eliminated by SD ambiguities between satellites, the integer property of the SD ambiguities between satellites will be retrieved.

Table 1 Quality control strategies for UCPPP AR

Terms	Threshold
Elevation	15°
Fractional part of SD WL ambiguity	0.25 cycles
Standard deviation of SD WL ambiguity	0.25 cycles
Successful rate of SD WL ambiguity rounding	0.99
Fractional part of SD NL ambiguity	0.25 cycles
Standard deviation of SD NL ambiguity	0.25 cycles
Successful rate of SD NL ambiguity bootstrapping	0.99
Critical value of the ratio test for SD NL AR	3.0
Critical value of the fixed failure-rate ratio test (FFRT) for SD NL AR	0.001
Minimum number of fixed ambiguities	4

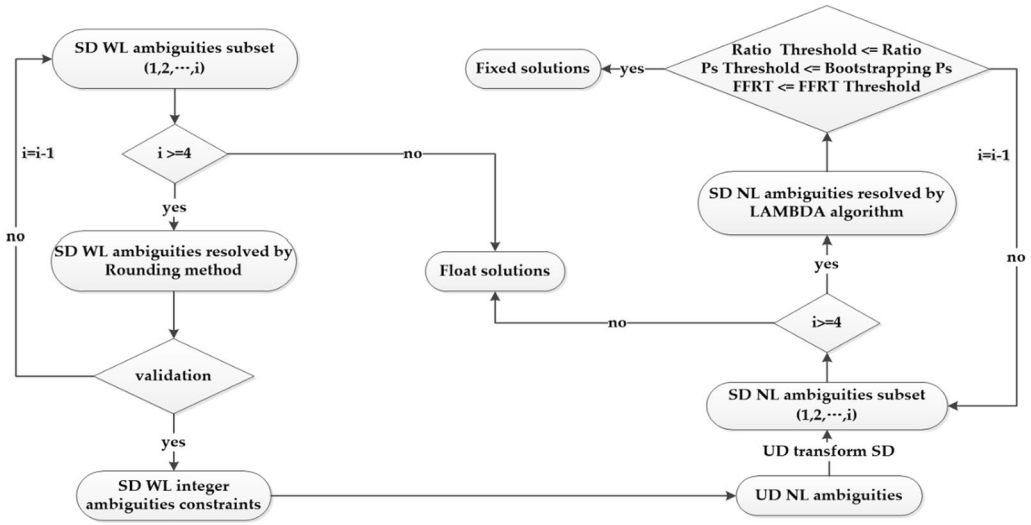

Fig. 1 Flowchart of two-step partial UCPPP AR

At the reference sites, the SD WL ambiguities are fixed first. After the SD WL ambiguities have been fixed successfully, the fixed SD WL ambiguities are considered as constraints to update the floating solutions. Afterwards, the UD NL ambiguities are extracted from the floating solutions updated with the fixed SD WL ambiguities. The UD NL ambiguities can be transformed to SD NL ambiguities. After the SD NL ambiguities have been fixed successfully, the state vector of the floating solutions is updated with the fixed SD NL ambiguities again.

The state vector of the floating solutions can be updated with the following formula (Li et al. 2014a).

$$\begin{cases} \overset{\vee}{X} = \hat{X} - Q_{\hat{X}\hat{N}} S^{\mathrm{T}} \left(S Q_{\hat{N}\hat{N}} S^{\mathrm{T}} \right)^{-1} \left(\hat{N}_{\mathrm{SD}} - \overset{\vee}{N}_{\mathrm{SD}} \right) \\ Q_{\overset{\vee}{X}\overset{\vee}{X}} = Q_{\hat{X}\hat{X}} - Q_{\hat{X}\hat{N}} S^{\mathrm{T}} \left(S Q_{\hat{N}\hat{N}} S^{\mathrm{T}} \right)^{-1} S Q_{\hat{N}\hat{X}} \end{cases}, \tag{5}$$

where $\hat{N}_{\mathrm{SD}}$ represents the SD floating ambiguity that can be accurately fixed; $\overset{\vee}{N}_{\mathrm{SD}}$ is the optimal integer solution for SD floating ambiguity; $Q_{\hat{N}\hat{N}}$ denotes the UD floating ambiguity covariance matrix that determines the structure of $\hat{N}_{\mathrm{SD}}$; $Q_{\hat{X}\hat{N}}$ represents the covariance matrix involving the relationship between the UD floating ambiguity and the remaining estimated parameters of the floating solutions; S represents the transformation matrix that maps from the UD floating ambiguity to the SD floating ambiguity; $\hat{X}$ and $\overset{\vee}{X}$ denote the vector of both the floating and the fixed solution containing the remaining unknowns, respectively; $Q_{\hat{X}\hat{X}}$ and $Q_{\overset{\vee}{X}\overset{\vee}{X}}$ are the covariance matrix of both the floating and the fixed solution containing the remaining unknowns, respectively.

After the ionospheric corrections have been generated from the reference network, the interpolation method is recommended for many algorithms (Han 1997; Wanninger 1995; Gao et al. 1997). Because the variance of interpolated errors mainly depends on the distance between stations, we interpolated the slant ionospheric delay by applying the distance-based linear interpolation method (DIM) for the same satellite to enhance the convergence performance of PPP-RTK. Throughout the DIM algorithm, slant ionospheric correction of a satellite s visible by the user component is interpolated from n reference stations and weighted by the inverse distance between the reference network and the user components. The interpolated slant ionospheric correction can be calculated as follows:

$$I_{\mathrm{u}}^{\mathrm{s}} = \sum_{i=1}^{n} \frac{1}{d_i} \tilde{I}_i^{\mathrm{s}} \Big/ \sum_{i=1}^{n} \frac{1}{d_i} = \left(\sum_{i=1}^{n} \frac{1}{d_i} I_i^{\mathrm{s}} - \frac{f_2^2}{f_1^2 - f_2^2} \sum_{i=1}^{n} \frac{1}{d_i} \mathrm{DCB}_{P_1-P_2,i}^{\mathrm{r}} \right) \Big/ \sum_{i=1}^{n} \frac{1}{d_i}, \tag{6}$$

where d_i denotes the distance between the reference station and user station, $I_{\mathrm{u}}^{\mathrm{s}}$ represents the interpolated slant ionospheric correction of satellite s visible to the user, I_i^{s} is the pure slant ionospheric delay of satellite s visible to the user and reference station i, $\tilde{I}_i^{\mathrm{s}}$ is the slant ionospheric delay containing the I_i^{s} and receiver DCBs from reference

station i; $\mathrm{DCB}^{\mathrm{r}}_{P_1-P_2,i}$ represents the receiver DCBs at reference station i, and n indicates the number of reference stations.

In the case of the stochastic parts, the variance of the user's interpolated ionospheric delays is related to two factors. On the one hand, the noise and multiple paths errors of the reference network may cause the errors to affect the precision of the estimated ionospheric delays. On the other hand, the interpolated error also has an influence on the precision of interpolated ionospheric corrections. Normally, the variance mainly depends on the distance between the reference network and the user station. Thus, the variance $P^{\mathrm{s}}_{\mathrm{u}}$ following $I^{\mathrm{s}}_{\mathrm{u}}$ can be represented as follows:

$$P^{\mathrm{s}}_{\mathrm{u}} = 1 \Big/ \sum_{i=1}^{n} \frac{1}{P^{\mathrm{s}}_{i}}, \text{ with } P^{\mathrm{s}}_{i} = \delta^{\mathrm{s}2}_{i} + d^{2}_{i}\mu^{2} / \sin^{2} \mathrm{el}^{\mathrm{s}}_{i}, \tag{7}$$

where $P^{\mathrm{s}}_{\mathrm{u}}$ is the variance of $I^{\mathrm{s}}_{\mathrm{u}}$, $\delta^{\mathrm{s}2}_{i}$ is the precision of the slant ionospheric delay of satellite s visible to reference station i, $\mathrm{el}^{\mathrm{s}}_{i}$ indicates the elevation angle of satellite s, and $\mu = 1.04$ mm/km is adopted as the empirical scale factor (Li et al. 2014b; Odijk 2000; Liu and Lachapelle 2002).

Figure 2 shows the geometric relationship between the reference network and the user's position when using the DIM algorithm to interpolate the slant ionospheric delays. The slant ionospheric correction of a given satellite (s) visible to the user components can be interpolated by utilizing the slant ionospheric delays of the same satellite visible to the reference stations. Moreover, for the user, the processes of generating slant ionospheric correction and variance are carried out epoch by epoch. When the slant ionospheric correction/variance of a given satellite is available for a certain epoch, the user can apply it to improve the convergence performance of PPP-RTK.

At the user's position, the UCPPP model can be enhanced by applying ionospheric correction so that the convergence performance can be improved. The interpolated slant ionospheric corrections derived from the reference network are imported as virtual observations to accelerate the ambiguity resolution of PPP. Specifically, the UCPPP model with additional slant ionospheric constraint information can be expressed as:

$$\begin{cases} P_{\mathrm{u},1} = \rho_{\mathrm{u}} + c\widetilde{\mathrm{dt}}^{\mathrm{r}}_{\mathrm{u}} + T_{\mathrm{u}} + \tilde{I}_{\mathrm{u},1} + \varepsilon_{P_1} \\ P_{\mathrm{u},2} = \rho_{\mathrm{u}} + c\widetilde{\mathrm{dt}}^{\mathrm{r}}_{\mathrm{u}} + T_{\mathrm{u}} + \gamma_2\tilde{I}_{\mathrm{u},1} + \varepsilon_{P_2} \\ L_{\mathrm{u},1} = \rho_{\mathrm{u}} + c\widetilde{\mathrm{dt}}^{\mathrm{r}}_{\mathrm{u}} + T_{\mathrm{u}} - \tilde{I}_{\mathrm{u},1} + \lambda_1\tilde{N}_{\mathrm{u},1} + \varepsilon_{L_1} \\ L_{\mathrm{u},2} = \rho_{\mathrm{u}} + c\widetilde{\mathrm{dt}}^{\mathrm{r}}_{\mathrm{u}} + T_{\mathrm{u}} - \gamma_2\tilde{I}_{\mathrm{u},1} + \lambda_2(\tilde{N}_{\mathrm{u},1} + \tilde{N}_{\mathrm{u},w}) + \varepsilon_{L_2} \\ \tilde{I}_{\mathrm{u},1} - \tilde{I}_{\mathrm{u},1,\mathrm{net}} = w_I, w_I \sim N(0, \sigma^2_{w_I}) \end{cases}, \tag{8}$$

where $\tilde{I}_{\mathrm{u},1,\mathrm{net}}$ and $\sigma^2_{w_I}$ represent the slant ionospheric correction interpolated from the network component and its corresponding variance, obtained from Eqs. (6) and (7), respectively; w_I denotes the difference between the

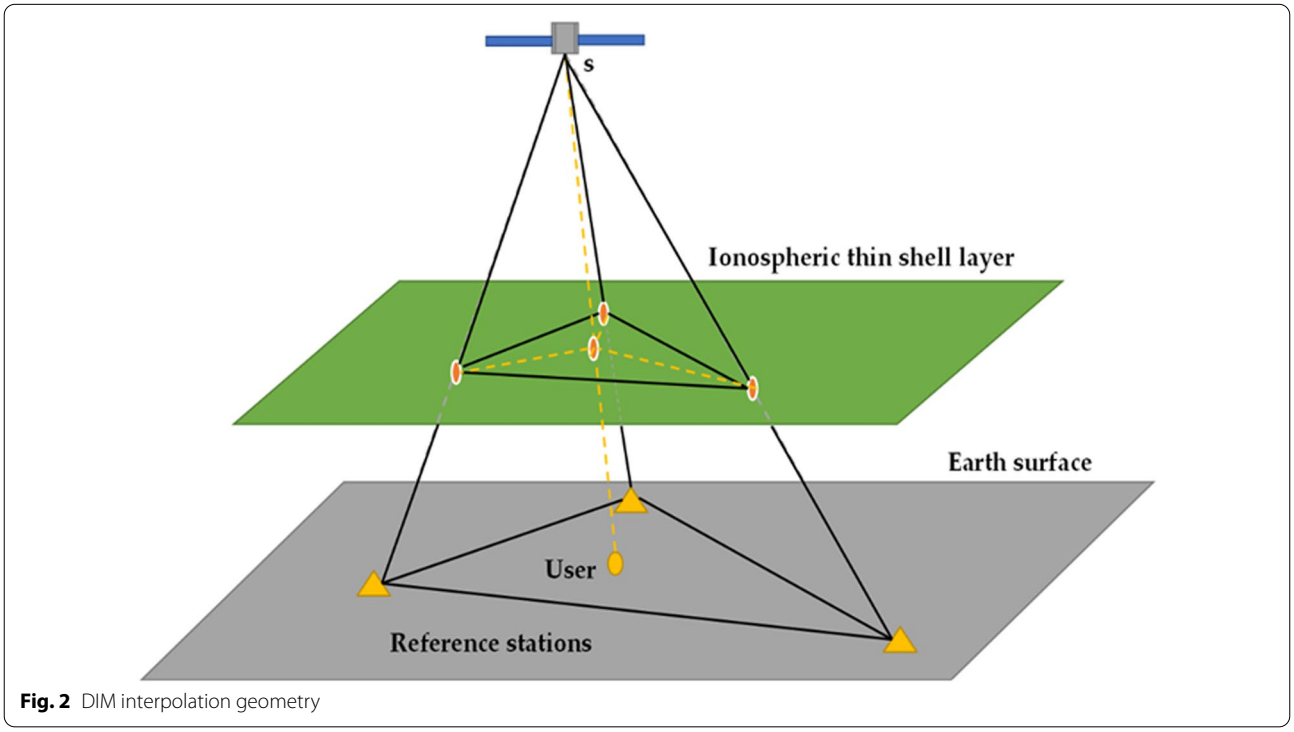

Fig. 2 DIM interpolation geometry

estimated slant ionospheric delay from the user component and interpolated slant ionospheric correction from the reference network.

Considering the above ionospheric virtual observations, we can extend the UCPPP function model of Eq. (3) to compensate for the variations in the estimated ionospheric delays in the PPP-RTK platform of the user components. Similarly, the stochastic model of UCPPP can be extended as well, as presented in Eq. (9):

$$Q_{\mathrm{UC}} = \mathrm{blkdiag}\left(Q_{P_{\mathrm{u}}P_{\mathrm{u}}}, Q_{L_{\mathrm{u}}L_{\mathrm{u}}}, Q_{w_I w_I}\right), \text{ with } Q_{w_I w_I} = \sigma_{w_I}^2 E, \tag{9}$$

where $Q_{P_{\mathrm{u}}P_{\mathrm{u}}}$ and $Q_{L_{\mathrm{u}}L_{\mathrm{u}}}$ represent the variance–covariance matrix of both the original pseudo-range and the carrier phase observations, respectively; $Q_{w_I w_I}$ represents the variance–covariance matrix of slant ionospheric correction for the user components; and E is the identity matrix. The notation blkdiag denotes a block diagonal matrix.

PPP-RTK platform design

In this study, we used a modified version of the precise point positioning with integer and zero-difference ambiguity resolution demonstrator (PPP-WIZARD) software as the PPP-RTK platform to carry out the experiments. The PPP-WIZARD software was developed by the Centre National d'Etudes Spatiales (CNES) to realize real-time PPP AR (Laurichesse and Privat 2015). The PPP-RTK platform was developed in C/C++. This platform mainly contains a network component for slant ionospheric delay estimation and a user component for augmented PPP AR with interpolated slant ionospheric correction. Figure 3 shows the PPP-RTK platform's structure including the network and user component. Because the structure of the network and user components was consistent, except for the estimation strategies of the coordinates and ionosphere parameters, we describe the common functionalities.

First, the configuration file for PPP-RTK network data processing needs to be read. Afterwards, the GNSS observations, precise GNSS orbits, clocks, OSB products, the IGS antenna correction file, and the station coordinate file are required as input to the software of the network component. During data processing, epoch by epoch, we fixed the coordinates of the reference stations to improve the accuracy of the slant ionospheric delays and reduce the number of unknown parameters. Second, the measurement cleaning step mainly identifies and removes data errors, including large gross errors and cycle slips. The remaining steps are then carried

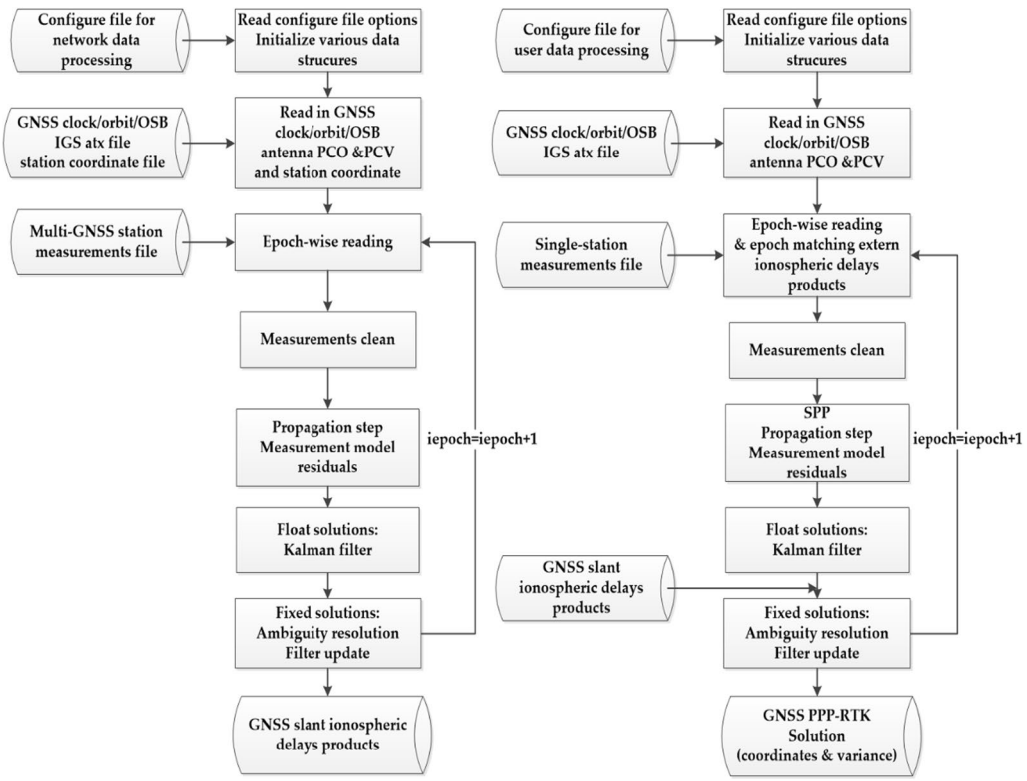

Fig. 3 Flowchart of the PPP-RTK platform of the network components (left) and the PPP-RTK platform of the user components (right)

out. Single point positioning (SPP) is used to compute the initial point coordinates. The propagation step is responsible for resolving the dynamic model (e.g., initial variance, and spectral density) of the state parameters. The observed-minus-computed (OMC) values can be obtained from the measurement model residuals. We applied the residuals of the OMC values to enable the Kalman filter to estimate the floating state vector. Third, UD WL ambiguities are extracted from the floating state parameters, and the SD WL ambiguities are formed by transforming the UD WL ambiguities. When the SD WL ambiguities have been fixed successfully, we can consider the SD WL integer ambiguities to be virtual observations for updating the floating solutions. Similarly, the UD NL ambiguities can be derived from the floating solutions updated with the fixed SD WL ambiguities. When the SD NL ambiguities have been fixed by the LAMBDA algorithm, the state parameters of the floating solutions will be updated with the fixed SD NL ambiguities. Finally, the slant ionospheric delays can be derived from the floating solutions updated with the fixed SD WL and the fixed SD NL ambiguities in succession. At the user end, the station coordinates need to be estimated to investigate the performance of PPP-RTK. Slant ionospheric delays interpolated by the DIM method are imported into the PPP-RTK user platform epoch by epoch. When the slant ionospheric corrections/variances have been obtained, we can take the slant ionospheric corrections as the virtual observations to enhance the model strength of the floating solutions and improve the convergence performance of PPP-RTK.

Results

A medium-scale network

In this part, the data selection and processing strategies for the reference network and the user components are introduced. We then assessed the accuracy of the slant ionospheric corrections by comparing the ionospheric corrections interpolated from the reference network with the user's results retrieved in the same manner as the network component. Finally, we investigated the convergence performance of PPP-RTK in pseudo-kinematic mode.

Data selection and processing strategies

To validate the convergence performance of PPP-RTK, five stations were used for the experiments. These stations belong to the European reference frame (EUREF) Permanent GNSS Network (EPN). Four stations (HETT, SAVU, TORN, and KUU2) were considered to be regional augmentation stations, and the station SOD3 was regarded as a user station. The five stations were equipped with the Javad-type receivers and capable of tracking GNSS satellites. The distribution of the stations is shown in Fig. 4. The average distance between the reference network sites and the user station was about 165 km. This indicates that this network is a medium-scale network.

The geomagnetic Kp index was determined by the GeoForschungsZentrum (GFZ) data services (Matzka et al. 2021a, b). The disturbance storm (Dst) was obtained from the international service of geomagnetic indices (ISGI) (Kauristie et al. 2017). The distribution of the Kp index and Dst from days 082 to 083 is demonstrated in Fig. 5. We can see that the Dst roughly varied from −30 to 10 nT and the Kp index varied from approximately 0 to 4, which indicates medium ionospheric disturbance during the experimental period (Matzka et al. 2021a).

For PPP-RTK data processing for both the network and the user components, the GPS L1/L2 and Galileo E1/E5a observations with a 30-s sample interval were used. Furthermore, we applied the final 5 min of the GFZ satellite orbits, 30-s satellite clocks, earth rotation parameters (ERPs), and the corresponding OSBs products provided by CNES (Laurichesse and Blot 2016). The absolute antenna phase center was corrected (Schmid et al. 2016). The cutoff elevation angle was set to 10°. An elevation-dependent weighting strategy was utilized to reduce the impact of both the atmospheric errors and multipath errors. The standard deviation was 0.3 m and 3 mm for the pseudo-range and carrier phase observations in the zenith direction, respectively. The parameter settings of the standard deviation can be considered as an appropriate choice in most cases (Li et al. 2008). An equal weighting strategy was applied to the GPS

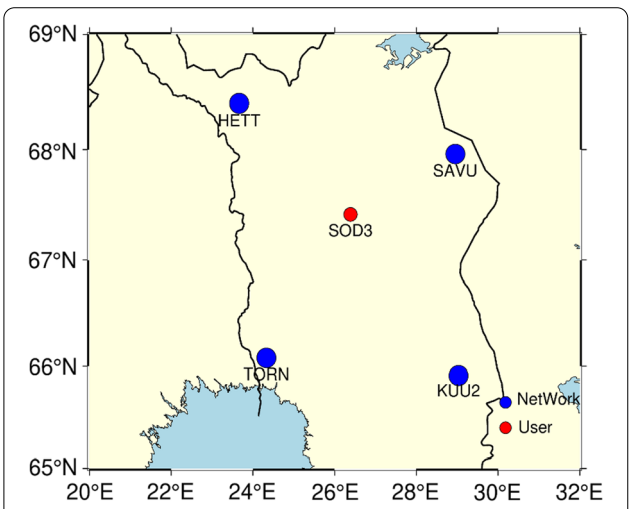

Fig. 4 Distribution of the GPS/Galileo stations from days 082 to 083 in 2021. The blue circles indicate reference stations, and the red circle denotes the user station

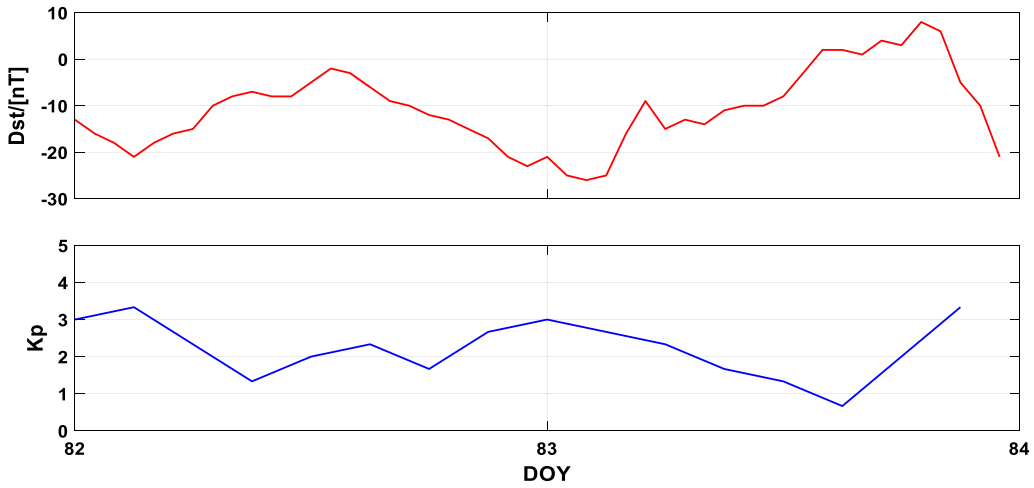

Fig. 5 Distribution of the Kp index and Dst from DOY 082 to 083 in 2021

and Galileo observations. Meanwhile, we corrected the effects of both phase wind-up and station displacement (Wu et al. 1993; Petit et al. 2010). The dry component of zenith troposphere delays was corrected by applying an a priori Saastamoinen model (Saastamoinen 1972), and the global mapping function (GMF) (Boehm et al. 2006) was employed as a mapping function. Meanwhile, the wet component of the zenith troposphere delays was modeled as a random walk process, in which the spectral density was empirically assumed to be $5 \times 10^{-5}\mathrm{m}/\sqrt{\mathrm{s}}$ (Li et al. 2020).

Figure 6 presents the number of satellites and the position dilution of precision (PDOP) of the user components. The average number of satellites was 10.96 and 19.26 for both the GPS-only and GPS + Galileo observations, respectively. The average values of PDOP were 2.38 and 1.56 for the GPS-only and combined GPS + Galileo observations, respectively. The PDOP values of GPS alone were less than 4 most times, while those of the integrated GPS and Galileo observations were mostly less than 2.

Performance of ionospheric corrections

In this section, the user station SOD3 was regarded as an additional reference station for estimating the UD slant ionospheric delays. The UD slant ionospheric delays of

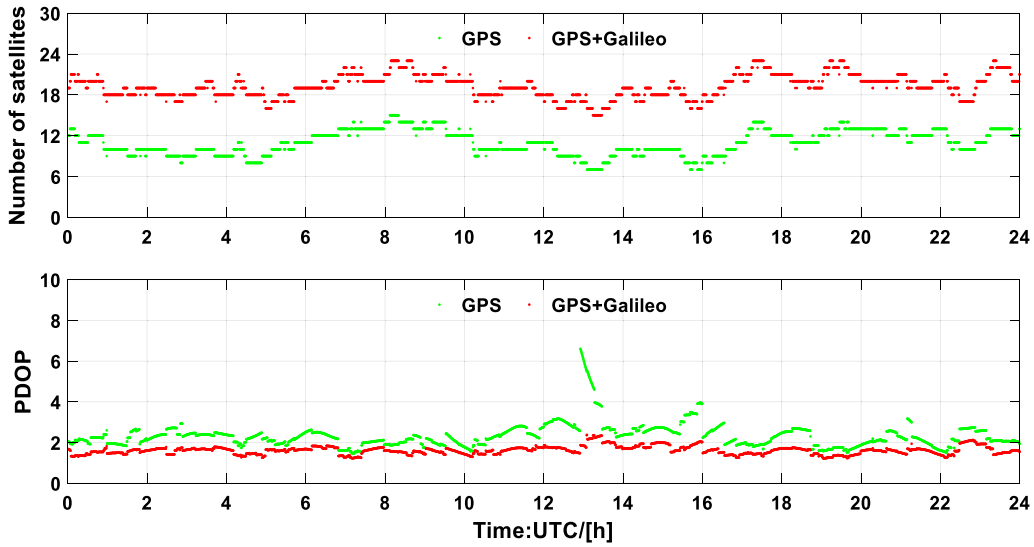

Fig. 6 Number of satellites (top) and PDOP (bottom) on DOY 082, 2021

the user station were used for assessing the slant ionospheric corrections. The slant ionospheric corrections were interpolated from the other four reference stations. Unfortunately, UD slant ionospheric delays are usually contaminated by the receiver DCBs. To eliminate the impact of receiver DCBs, it is reasonable to transform the UD slant ionospheric delays into the satellite-difference slant ionospheric delays. This transformation is implemented in two steps for the UD slant ionospheric delays of both the server and the user components simultaneously. Specifically, the first step is to select the reference satellite with the highest elevation angle to find a single difference from other satellites in the same satellite system. The second step is to find the difference between the user's SD slant ionospheric delays and the network-interpolated SD slant ionospheric corrections. Both of them are derived from Step 1 and follow the principle of selecting the same satellite pair and the same time. In addition, the accuracy of the slant ionospheric corrections in other satellite systems should be investigated as well.

Based on the above considerations, slant ionospheric corrections derived from the GPS and Galileo constellation can be compared and analyzed. Figure 7 shows the error distribution of the interpolated SD slant ionospheric corrections in detail. For the SD GPS ionospheric residuals, the proportions within 0.15 total electron content units (TECU) and 0.30 TECU were 73.1% and 85.2%, respectively. This means that, converted to L_1, 85.2% of the ionospheric residuals were less than 5 cm. The accuracy of the slant ionospheric corrections can significantly accelerate the initialization of the PPP (Geng et al. 2010b). Similarly, proportions of 65.3% and 81.7% for SD Galileo ionospheric residuals were obtained under the conditions of 0.15 and 0.30 TECU, respectively.

Performance of PPP-RTK

In this section, the convergence performance of the user components was investigated as follows. To obtain enough samples to assess the convergence performance, the observations were processed every 1 h to assess the convergence performance of PPP-RTK. If the SD WL and SD NL ambiguities were fixed successfully, and the positioning errors of both the horizontal and vertical components were less than 4 cm and 10 cm, respectively, the fixed solutions could be achieved successfully (Li et al. 2020). It is worth mentioning that the observations in the first 1 h in all conditions were excluded to ensure that ambiguities at reference sites had been resolved reliably. Specifically, the 50th and 90th percentile curves based on all 46 datasets were used to demonstrate the convergence performance of PPP-RTK. The convergence time of PPP-RTK is defined as the time to achieve a certain level of positioning accuracy. Specifically, in this work, it means that the horizontal and vertical positioning errors are less than the threshold of 10 cm, respectively. The positioning error is the difference between the estimated positions and true coordinates. What's more, only when the positioning error of horizontal and vertical components of 20 consecutive epochs after this epoch is less than 10 cm, the PPP-RTK can be considered to convergence at this epoch (Li and Zhang 2014).

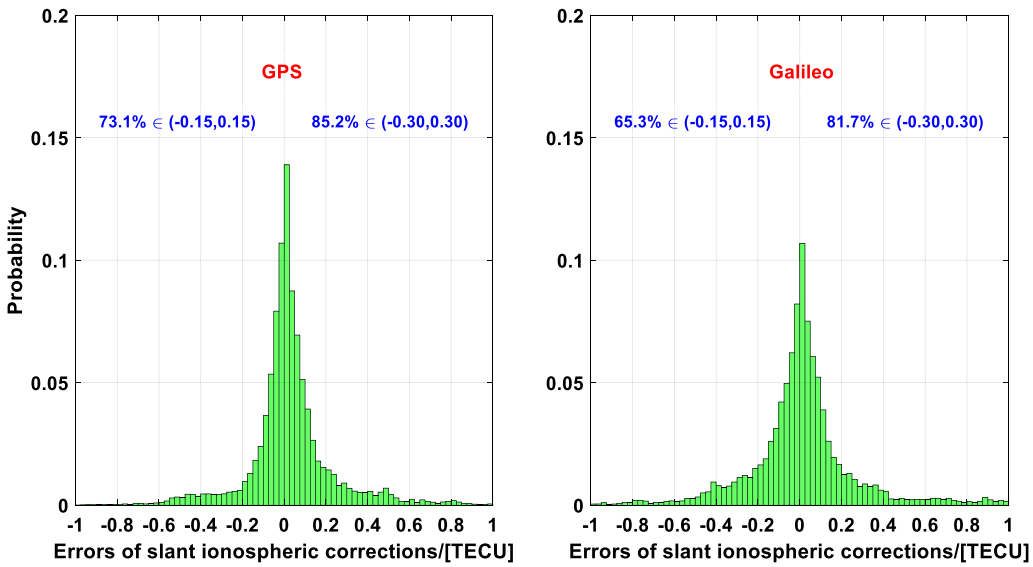

Fig. 7 Error distribution of the SD slant ionospheric delays in different satellite systems (left panel: GPS; right panel: Galileo)

Figure 8 and Table 2 depict the 50th and 90th percentile convergence performance of the PPP-RTK user components. Furthermore, we investigated the convergence performance of both GPS alone and integrated GPS + Galileo. For the 50th percentile situations, the convergence time, in the horizontal and vertical components, respectively, reduced by 1.0 and 1.5 min for the GPS-only observations, and by 0.5 and 1.0 min for the combined GPS + Galileo observations. Compared with GPS-only PPP-RTK, PPP-RTK based on GPS + Galileo observations reduced the convergence time by an average of 40%. From the results of the 90th percentile, we also found that the convergence time of PPP-RTK using GPS observations was 2.5 and 3.0 min in the horizontal and vertical components, respectively. When utilizing GPS + Galileo observations, the PPP-RTK convergence times of the horizontal and vertical components improved by 20% and 16.7%, respectively.

The convergence performance of GPS-only PPP-RTK was revealed in Psychas and Verhagen (2020). For the 50th percentile positioning errors of the horizontal component, Psychas and Verhagen (2020) took 1.0 and 1.5 min to achieve the 10 cm threshold, in terms of the networks with a spacing of 68 and 115 km. Our results are the same as those of the networks with 68 km and 115-km spacing at a 50% confidence level. For the 90th percentile positioning errors, the convergence times of networks with 68 and 115-km spacing in the study by Psychas and Verhagen (2020) were approximately 5.0 and 10.0 min, in terms of the horizontal component. By comparing these results, we can see that the 90th percentile horizontal positioning errors of GPS-only PPP-RTK can still achieve better than 10-cm convergence within 2.5 min when slant ionospheric corrections derived from the network with 165-km spacing were utilized. Banville et al. (2014) also investigated fast PPP convergence performance using regional slant ionospheric corrections. Their results demonstrated that when using GPS-only ionospheric corrections derived from the network with 150-km spacing, the convergence better than the 10-cm threshold could be obtained within 5 min.

Table 2 Convergence time of PPP-RTK user components for the medium-scale network at the 50% and 90% confidence levels

Method	GPS		GPS + Galileo	
	Horizontal (min)	Vertical (min)	Horizontal (min)	Vertical (min)
PPP-RTK (50%)	1.0	1.5	0.5	1.0
PPP-RTK (90%)	2.5	3.0	2.0	2.5

It can be seen from the comparison of the results that our results are reliable and valid. However, we also should note that the convergence performance of PPP-RTK using regional ionospheric corrections was affected by many factors, such as satellite geometry, the quality of the observations, and ionospheric conditions. As Banville said, the ambiguity resolution of a PPP algorithm should exclude wrongly fixed ambiguities to ensure that ambiguity resolution is accurate, and the precision of ionospheric corrections should actually reflect their deficiencies in

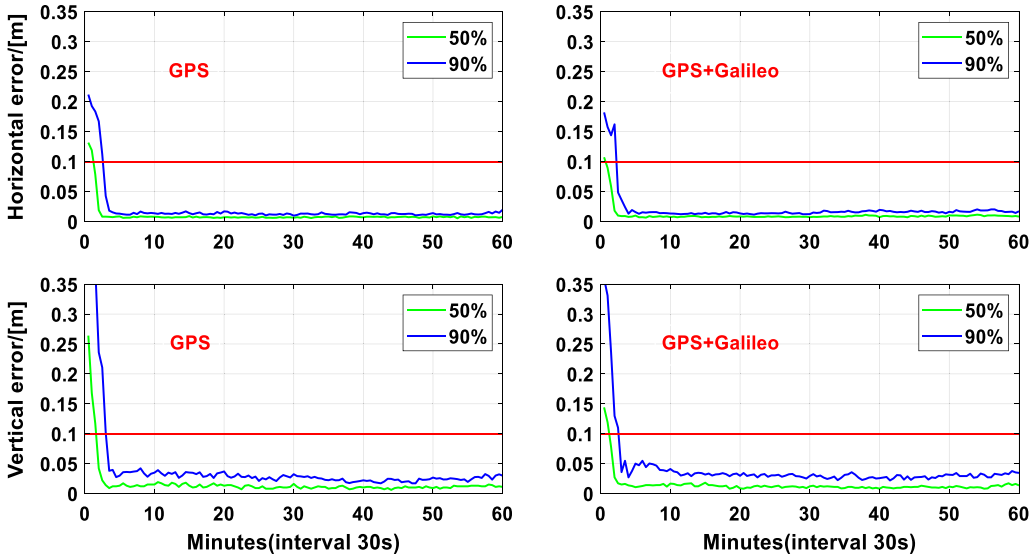

Fig. 8 Convergence performance of PPP-RTK user components for the medium-scale network at the 50% and 90% confidence levels. Top panel: horizontal error; bottom panel: vertical error. Left panel: GPS; right panel: GPS + Galileo

UCPPP model to enhance the UCPPP model strength to accelerate the ambiguity fixing.

A small-scale network

In this section, first, we processed a National Oceanic and Atmospheric Administration (NOAA) Continuously Operating Reference Stations (CORS) Network (NCN), whose processing strategies are the same as those of the network with 165-km spacing. We then evaluated the accuracy of the slant ionospheric corrections interpolated from the reference network. Finally, the convergence performance of PPP-RTK was implemented for validation in pseudo-kinematic mode.

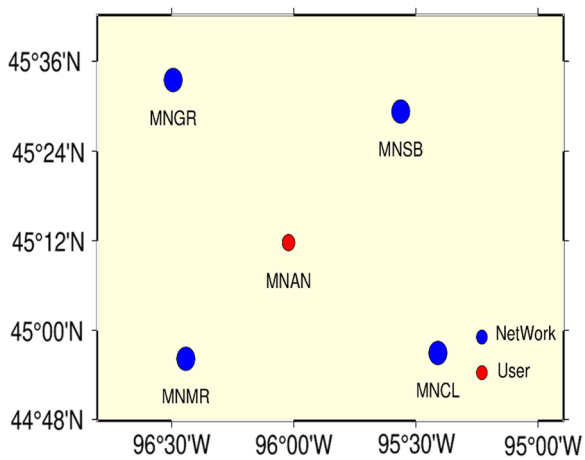

Fig. 9 Distribution of the GPS/Galileo stations from days 082 to 083 in 2021. The blue circles indicate the reference stations and the red circle denotes the user station

Data selection and processing strategies

To investigate the convergence performance of PPP-RTK, five stations were utilized to process the GNSS data. Four reference stations (MNGR, MNSB, MNMR, and MNCL) were considered as reference stations for generating slant ionospheric corrections, and the MNAN station was regarded as the user station. The five stations were equipped with Trimble-type receivers and capable of tracking GNSS satellites. The distribution of the GNSS network is shown in Fig. 9. We applied 2 days (days 082 and 083 of 2021) of GPS L1/L2 and Galileo E1/E5a observations with a 30-s sample to carry out PPP-RTK in pseudo-kinematic mode. The average distance between the reference network sites and the user station was about 50 km. The network of this scale indicates a small-scale network.

Performance of ionospheric corrections

In this section, the user station MNAN was considered as an additional reference station for obtaining the UD slant ionospheric delays. The slant ionospheric delays of the user station were used to evaluate the UD slant ionospheric corrections. The slant ionospheric corrections were interpolated from the reference network. Due to the receiver DCBs remaining in the ionospheric delays, we used the SD operators on the ionospheric delays to remove the impacts of the receiver DCBs. The specific assessment method is described in the previous section.

The error distribution of the interpolated SD ionospheric corrections is depicted in Fig. 10. In terms of the SD slant ionospheric residuals of the GPS constellation, the proportion within 0.15 TECU is 92.2%, while that

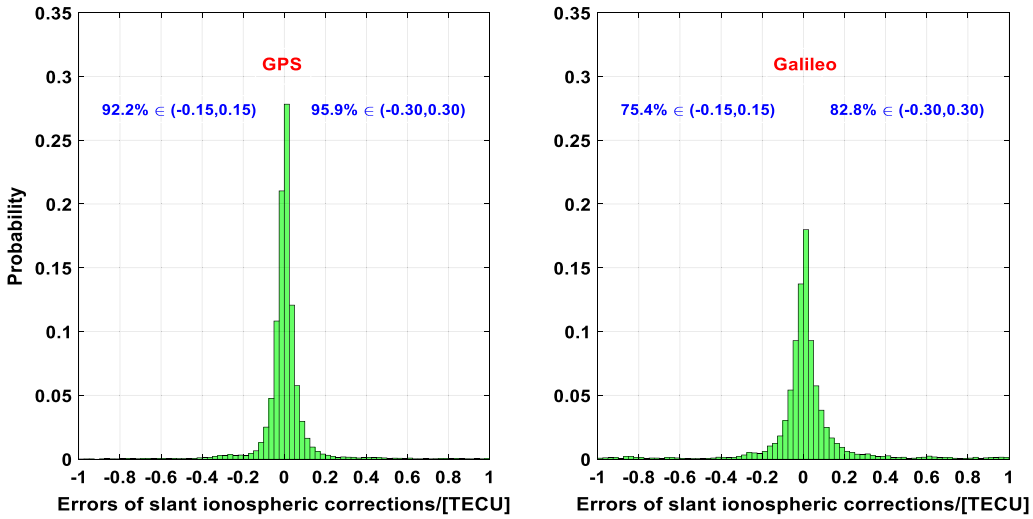

Fig. 10 Error distribution of the SD slant ionospheric delays in different satellite systems (left panel: GPS; right panel: Galileo)

within 0.30 TECU is 95.9%. In the case of the Galileo scenario, proportions of 75.4% and 82.8% were obtained under the conditions of 0.15 and 0.30 TECU, respectively. Comparing Figs. 7 and 10, we can see that the proportions of SD ionospheric residuals in small-scale networks are higher than those of medium-scale networks under the conditions of 0.15 and 0.30 TECU, whether the GPS and Galileo constellation is used. This may be because the accuracy of the ionospheric delays has a strong correlation with the distance between stations (Liu and Lachapelle 2002). The longer distance between stations, the weaker the correlation of the ionospheric delays (Gao et al. 2021). Larger modeling errors of the ionospheric delays may be generated in a larger-scale network. This may be the reason why the proportions of SD ionospheric residuals generated from the medium-scale network were lower than those from the small-scale network. Of course, networks with different scales may require similar ionospheric conditions.

From Fig. 10, we can also find another situation, which the proportion of GPS SD slant ionospheric residuals in a certain range is higher than that of Galileo. A similar situation exists in Fig. 7, but their difference in Fig. 7 is slightly smaller than that in Fig. 10. To further study the reasons behind this phenomenon, we analyze the number of both ionospheric delays and fixed SD NL ambiguities, whether for reference network and user components. Due to the limited length of the article, we only present and analyze the limited results of both reference network and user components. Other situations are generally the same as those shown in this paper.

From Figs. 11 and 12, we can find that the number of Galileo ionosphere is less than that of GPS, whether for reference network station MNMR or user station MNAN. Furthermore, the number of Galileo NL resolved ambiguities is also less than that of the ionosphere. As we know, the more the number of resolved ambiguities and the better spatial geometry, the more significant the effect of improving the accuracy of positioning and other parameters to be estimated in the UCPPP model. On the contrary, if the number of resolved ambiguities is small, the accuracy of estimated parameters in the fixed solutions may not be well guaranteed. Hence, comparing Figs. 10, 11, and 12, it is suggested that the main reason for the large ionospheric residuals of Galileo is mainly due to the insufficient resolved number of NL ambiguities resulting in low ionospheric accuracy. Of course, many other potential factors that affect ambiguity fixing, e.g., data quality of Galileo, the accuracy of Galileo orbit/clock products, the corrections of receiver's PCOs and PCVs, and the defined weight strategies between GPS observations and Galileo observations. Finally, we believe that these are temporary problems. With the completion of Galileo's global network deployment and the further improvement of corresponding models and algorithms, the performance of Galileo's ionospheric residuals will be close to GPS.

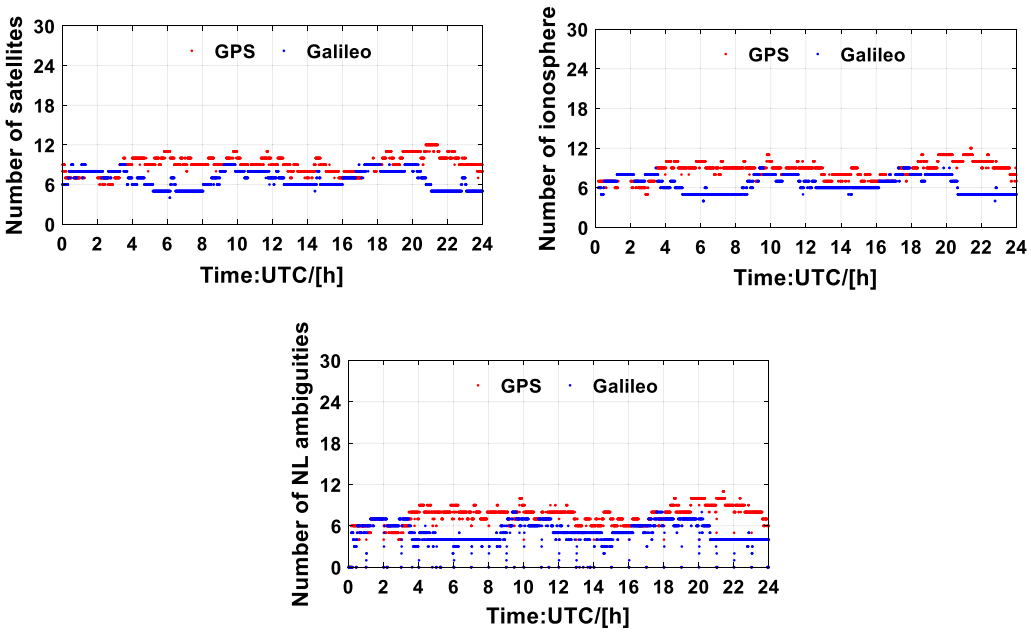

Fig. 11 Number of satellite, number of fixed SD NL ambiguities, and number of estimated ionospheric delays from MNAN station on DOY 082, 2021

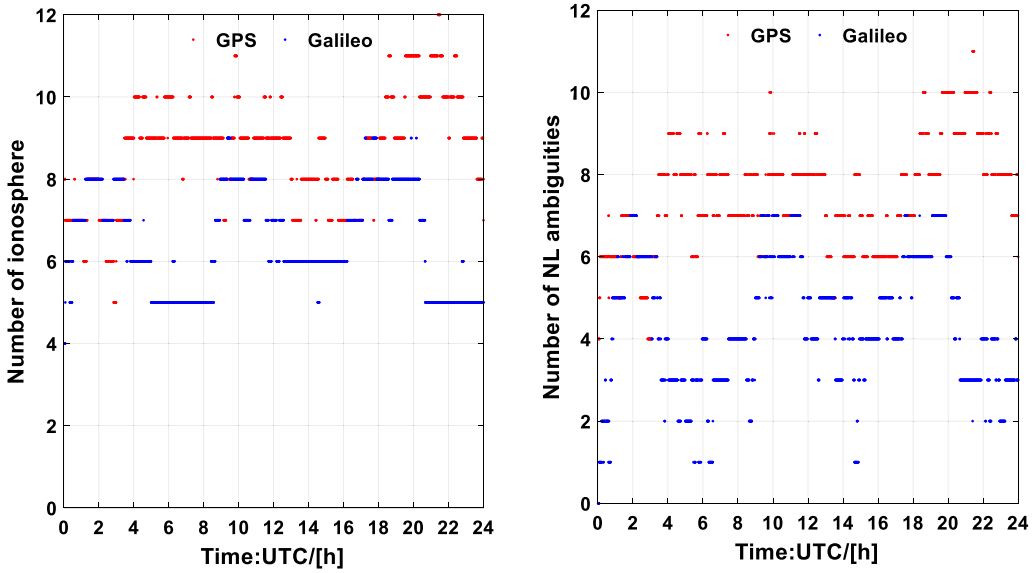

Fig. 12 Number of fixed SD NL ambiguities and the number of estimated ionospheric delays from MNMR station on DOY 082, 2021

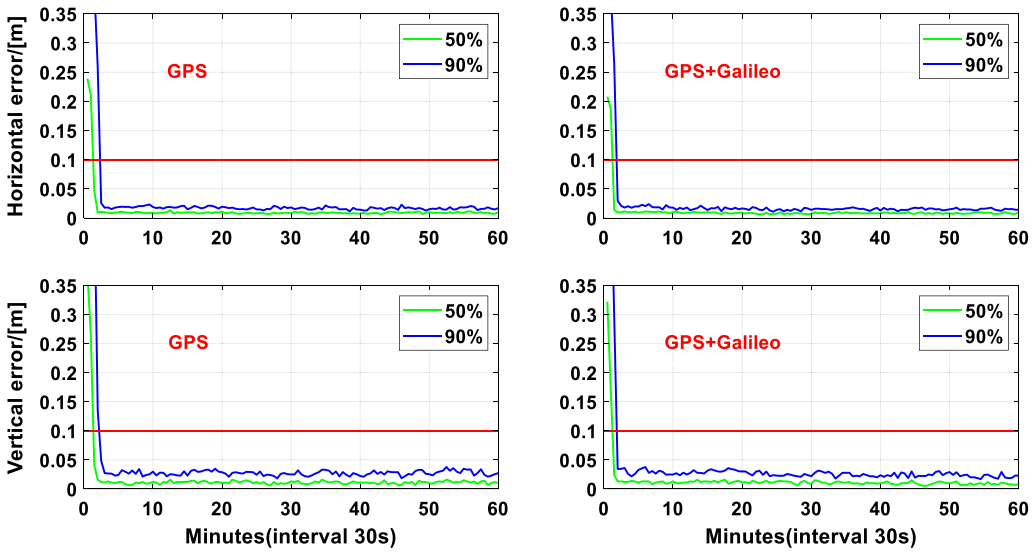

Fig. 13 Convergence performance of PPP-RTK user components for the small-scale network at the 50% and 90% confidence levels. Top panel: horizontal error; bottom panel: vertical error. Left panel: GPS; right panel: GPS + Galileo

Performance of PPP-RTK

We took the 50th and 90th percentile positioning errors of both the horizontal and vertical components as indicators to investigate the convergence performance of PPP-RTK for GPS alone and integrated GPS + Galileo observations. Figure 13 and Table 3 show the convergence performance of PPP-RTK for the 50th and 90th percentiles of the horizontal and vertical positioning errors in detail. For the 50th percentile scenario, the

Table 3 Convergence time of PPP-RTK user components for the small-scale network at the 50% and 90% confidence levels

Method	GPS		GPS + Galileo	
	Horizontal (min)	Vertical (min)	Horizontal (min)	Vertical (min)
PPP-RTK (50%)	1.0	1.0	1.0	1.0
PPP-RTK (90%)	2.0	2.0	1.5	1.5

integrated GPS + Galileo observations had no obvious advantage over the GPS-only observations in terms of the convergence performance of the horizontal and vertical components. This indicates that the constraints of ionospheric corrections can significantly reduce the correlation between the positioning parameters and other estimated parameters in GPS-only PPP-RTK of the user components. Hence, the Galileo observations did not reduce the convergence time at the 50% confidence level. On the contrary, the horizontal and vertical convergence time reduced from 2.0 min for GPS-only PPP-RTK to 1.5 min for integrated GPS + Galileo PPP-RTK at the 90% confidence level. The convergence time could be shortened by 25% by using GPS and Galileo observations.

To investigate the convergence performance of PPP-RTK in networks with different scales, we compared the PPP-RTK convergence time between the medium-scale network and the small-scale network. As far as the 90% confidence level was concerned, the average convergence time of the small-scale network was less than that of the medium-scale network. Therefore, it can be suggested that the convergence time of PPP-RTK is related to the scale of the reference network. The larger scale of the reference network, the longer the convergence time of the user components (Psychas and Verhagen 2020). The relationship between the convergence time of the user and the scale of the network has also been verified in analyses of the accuracy of the ionospheric corrections derived from networks with different scales (Gao et al. 2021). In terms of the larger-scale network, the convergence time was affected by the accuracy of the interpolated slant ionospheric corrections. Overall, although the scale of the reference network affected the convergence performance of PPP-RTK, our results suggest that the GPS-only PPP-RTK could achieve convergence in the horizontal direction within 2.0 and 2.5 min and the integrated GPS + Galileo PPP-RTK could achieve convergence in the horizontal direction within 1.5 and 2.0 min for the small-scale network and the medium-scale network, respectively.

Discussion

In this study, we investigated the convergence performance of GPS + Galileo PPP-RTK using two networks with different scales. As far as the accuracy assessment of the interpolated ionospheric corrections is concerned, for the network with 165-km spacing, the proportion of the GPS SD ionospheric residuals within 0.30 TECU was 85.2%, while that of the Galileo SD ionospheric residuals was 81.7%. For the network with 50-km spacing, the proportion of GPS SD ionospheric residuals within 0.30 TECU was 95.9%, while that of the Galileo SD ionospheric residuals was 82.8%. The difference in the proportions of SD ionospheric residuals between the 165-km network and the 50-km network was associated with the ionospheric modeling errors. The errors mainly depend on the distance between stations (Xiang et al. 2020). Meanwhile, it is also noted that the ionospheric parameters not only have uncertain random variations but also contain the receiver's DCBs. When different receiver types are used for the stations in the reference network, the interpolated slant ionospheric delays derived from can be affected due to the large differences of receiver's DCBs. Therefore, these ionospheric delays containing the receiver's DCBs may not be suitable for direct interpolation of ionospheric delays, because the relationship between the spatiotemporal variation characteristics of DCBs and the ionospheric delays needs further research. From the perspective of ionospheric modeling, the impact of the receiver's DCBs can be eliminated by using the SD ionospheric delays between satellites. However, as we know, the reference satellite can only be viewed by the reference network and user station within a certain range. When it exceeds a certain range, this method may be invalid for the ionospheric modeling of wide-area PPP-RTK. Hence, to maintain a high degree of self-consistency between the reference network and user component of PPP-RTK, the best strategy to resolve the receiver's DCBs is to apply the global ionospheric maps (GIMs), which are considered initial values to constrain the ionospheric parameters in UCPPP model. Therefore, the receiver's DCBs can be effectively separated from the slant ionospheric delays. Correspondingly, when the user utilizes the interpolated slant ionospheric delays, the receiver's DCBs can also be estimated in the UCPPP model, which does not affect the model strength of PPP-RTK. In addition to the effect of the receiver's DCBs, the condition of the observation, reference network scales may affect the degree of agreement between interpolated slant ionospheric delays derived from the reference network and self-estimated slant ionospheric delays estimated from user components. On the other hand, in this study, the DIM uses the empirical scale factor to compensate for the effect of inter-station distance on the accuracy of the interpolated ionospheric delays. Li et al. (2014b) gave a variable range of empirical scale factors from 0.3 to 3 mm/km. Odijk (2000) took 0.57 mm/km as the scale factor to research the Californian network. However, the empirical accuracy of interpolated ionospheric corrections may not effectively mitigate the impact of ionospheric delays in the UCPPP model. Hence, it is necessary to propose an ionospheric modeling method that is suitable for various networks of different scales and eliminates the impact of the receiver's DCBs. More importantly, this model should adequately reflect the random variation characteristics of the ionospheric delays.

In terms of the convergence performance of PPP-RTK, for the 165-km network, it took 2.5 and 2.0 min for the GPS-only and integrated GPS + Galileo observations to achieve the 10-cm threshold for the 90th percentile horizontal positioning errors. Using the slant ionospheric corrections derived from the network with 50-km spacing, the GPS-only, and integrated GPS + Galileo PPP-RTK achieved convergence in the horizontal direction within 2.0 and 1.5 min at the 90% confidence level. The PPP-RTK convergence time was further reduced by utilizing the GPS and Galileo observations together. Meanwhile, it has been noted that when the scale of the network becomes larger, the convergence time of PPP-RTK will become longer to some extent. This has already been verified in Psychas and Verhagen (2020). The GPS-only PPP-RTK using regional ionospheric corrections derived from the network with 165-km spacing achieved convergence in the horizontal direction within 2.5 min at the 90% confidence level. Similar results have also been found in Banville et al. (2014), which indicates our results are reliable. This suggests that our results may provide a reference for studying the convergence performance of multi-GNSS PPP-RTK based on networks with different scales.

Even though the expected results could be found, our study only concentrated on validation of the results by utilizing limited GPS/Galileo observations from two networks with different scales under medium ionospheric disturbance. Ionospheric delays have many complicated characteristics in time and space, which are not still fully known at present. Hence, new ideas require to be proposed for ionospheric modeling, especially for the wide-area slant total electron content (STEC) modeling algorithm. Furthermore, it is expected that the convergence performance of PPP-RTK can be further improved by using multi-GNSS and multi-frequency observations. Considering the above analysis, the modeling algorithm of STEC and the potential of multi-GNSS and multi-frequency for PPP-RTK should be comprehensively investigated in the future.

Conclusions

This contribution mainly investigates the convergence performance of PPP-RTK by using GPS and Galileo observations. To this end, the convergence performance of PPP-RTK was assessed by utilizing the GPS/Galileo observations from two networks with a large difference in their scale.

For the network with an average distance of about 165 km, 85.2% of the SD GPS ionospheric residuals were within 0.30 TECU, while 81.7% of the SD Galileo ionospheric residuals were within 0.30 TECU. In terms of the 50th percentile, the PPP-RTK convergence times in the horizontal and vertical directions were reduced from 1.0 and 1.5 min for the GPS alone observations to 0.5 and 1.0 min for the integrated GPS + Galileo observations. An average improvement of 40% could be obtained. Similarly, for the 90th percentile positioning errors of the horizontal and vertical components, the convergence times to be reduced from 2.5 and 3.0 min for the GPS-only observations to 2.0 and 2.5 min for the integrated GPS + Galileo observations, with an average improvement of 18.1%.

For the network with an average distance of about 50 km, 95.9% of the SD GPS ionospheric residuals were within 0.30 TECU, while 82.8% of the SD Galileo ionospheric residuals were within 0.30 TECU, respectively. The 90th percentile positioning errors of the horizontal and vertical components reduced the convergence times from 2.0 and 2.0 min for the GPS-only observations to 1.5 and 1.5 min for the integrated GPS + Galileo observations. An average improvement of 25% could be achieved.

Whether it is the accuracy of slant ionospheric delays or the convergence performance of PPP-RTK, the 50-km network showed obvious advantages. This is mainly because of the strong correlation between the ionosphere and the scale of the reference network. Meanwhile, it is noted that the integrated GPS and Galileo observations could further reduce the convergence time of PPP-RTK for the networks with 50 and 165-km spacing.

Abbreviations

PPP: Precise point positioning; AR: Ambiguity resolution; PPP-RTK: PPP real-time kinematic; GPS: Global Positioning System; GNSS: Global Navigation Satellite Systems; BDS: BeiDou Navigation Satellite System; RMS: Root-mean-square; Galileo: Galileo Satellite Navigation System; PCOs: Phase center offsets; PCVs: Phase center variations; IF: Ionospheric free; DCBs: Differential code biases; NL: Narrow-lane; WL: Wide-lane; OSBs: Observables specific signal biases; UPDs: Uncalibrated phase delays; SD: Single-difference; LAMBDA: Least-square ambiguity decorrection adjustent; ILS: Integer least-square; UD: Un-difference; DIM: Distance-based linear interpolation method; PPP-WIZARD: Precise point positioning with integer and zero-difference ambiguity resolution demonstrater; CNES: Centre National d'Etudes Spatiales; OMC: Observed-minus-computed; EUREF: European reference frame; EPN: European reference frame Permanent GNSS Network; GFZ: GeoForschungsZentrum; Dst: Disturbance storm; ISGI: International service of geomanetic indices; ERPs: Earth rotation parameters; GMF: Global mapping function; PDOP: Position dilution of precision; TECU: Total electron content units; NOAA: National Oceanic and Atmospheric Administration; CORS: Continuously Operating Reference Stations; NCN: National Oceanic and Atmospheric Administration Continuously Operating Reference Stations Network; STEC: Slant total electron content.

Acknowledgements

The authors are very grateful to thank three anonymous reviewers of this paper for their meaningful suggestions and comments. The GFZ, CNES Analysis Center, EUREF Permanent GNSS Network, and NCN are also appreciated for providing access to multi-GNSS products and multi-GNSS observations.

Authors' contributions

YZ performed the data processing and drafted the manuscript. ZX discussed and analyzed the data, critically revised the manuscript, and proof-read the submission. Both authors read and approved the final manuscript.

Authors' information
YZ is a Ph.D. candidate of Wuhan University. His current research is Multi-GNSS and Multi-frequency PPP-RTK and regional ionosphere modeling. ZX is a professor of Wuhan University. His current research involves GNSS precise point positioning and GNSS/INS.

Funding
This research was funded by the National Science Fund for Distinguished Yong Scholars (No. 41825009), the Changjiang Scholars Program.

Availability of data and materials
The precise orbit and clock products from GFZ and CNES are obtained at ftp://ftp.gfz-potsdam.de/pub/GNSS/products/mgex/ and https://www.ppp-wizard.net/products/POST_PROCESSED/; multi-GNSS observations are available through EUREF and NCN data centers (ftp://ftp.epncb.oma.be/pub/obs/; https://geodesy.noaa.gov/corsdata/rinex/).

Declarations

Ethics approval and consent to participate
Not applicable.

Competing interests
The authors declare that they have no competing interests.

Received: 4 January 2022 Accepted: 6 March 2022
Published online: 23 March 2022

References

Banville S, Collins P, Zhang W, Langley RB (2014) Global and regional ionospheric corrections for faster PPP convergence. J Inst Navig 61:115–124. https://doi.org/10.1002/navi.57
Banville S, Geng J, Loyer S et al (2020) On the interoperability of IGS products for precise point positioning with ambiguity resolution. J Geodesy 94:10. https://doi.org/10.1007/s00190-019-01335-w
Bertiger W, Desai SD, Haines B, Harvey N, Moore AW, Owen S, Weiss JP (2010) Single receiver phase ambiguity resolution with GPS data. J Geodesy 84(5):327–337
Blewitt G (1989) Carrier phase ambiguity resolution for the global positioning system applied to geodetic baselines up to 2000 km. J Geophys Res Atmos 94(B8):10187–10203
Boehm J, Niell A, Tregoning P, Schuh H (2006) Global mapping function (GMF): a new empirical mapping function based on numerical weather model data. Geophys Res Lett 33:L7304
Collins P (2008) Isolating and estimating undifferenced GPS integer ambiguities. In: Proceeding of ION NTM, pp 720–732
Cui B, Li P, Wang J et al (2021) Calibrating receiver-type-dependent wide-lane uncalibrated phase delay biases for PPP integer ambiguity resolution. J Geodesy 95:82. https://doi.org/10.1007/s00190-021-01524-6
Dong D, Bock Y (1989) Global positioning system network analysis with phase ambiguity resolution applied to crustal deformation studies in California. J Geophys Res 94(B4):3949–3966
Gao Y, Li Z, McLellan J (1997) Carrier phase based regional area differential GPS for decimeter-level positioning and navigation. In: Proceedings of the 10th international technical meeting of the satellite division of US Institute of Navigation, Kansas, MO, USA, 16–19 September 1997, pp 1305–1313
Gao W, Zhao Q, Meng X, Pan S (2021) Performance of single-epoch EWL/WL/NL ambiguity-fixed precise point positioning with regional atmosphere modelling. Remote Sens 13:3758. https://doi.org/10.3390/rs13183758
Ge M, Gendt G, Rothacher M et al (2008) Resolution of GPS carrier-phase ambiguities in precise point positioning (PPP) with daily observations. J Geodesy 82:389–399. https://doi.org/10.1007/s00190-007-0187-4
Geng J, Meng X, Dodson A, Teferle F (2010a) Integer ambiguity resolution in precise point positioning: method comparison. J Geodesy 84(9):569–581
Geng J, Meng X, Dodson AH et al (2010b) Rapid re-convergences to ambiguity-fixed solutions in precise point positioning. J Geodesy 84:705–714. https://doi.org/10.1007/s00190-010-0404-4
Geng J, Teferle FN, Meng X, Dodson AH (2011) Towards PPP-RTK: ambiguity resolution in real-time precise point positioning. Adv Space Res 47(10):1664–1673
Geng J, Shi C, Ge M, Dodson AH, Lou Y, Zhao Q, Liu J (2012) Improving the estimation of fractional-cycle biases for ambiguity resolution in precise point positioning. J Geodesy 86(8):579–589
Han S (1997) Carrier phase-based long-range GPS kinematic positioning. Ph.D. Thesis, School of Geomatic Engineering, The University of New South Wales, Sydney, Australia
Ji S, Chen W, Ding X, Chen Y, Zhao C, Hu C (2010) Ambiguity validation with combined ratio test and ellipsoidal integer aperture estimator. J Geodesy 84:597–604. https://doi.org/10.1007/s00190-010-0400-8
Kauristie K, Morschhauser A, Olsen N et al (2017) On the usage of geomagnetic indices for data selection in internal field modelling. Space Sci Rev 206:61–90. https://doi.org/10.1007/s11214-016-0301-0
Kouba J, Heroux P (2011) Precise point positioning using IGS orbit and clock products. GPS Solut 5:12–28. https://doi.org/10.1007/PL00012883
Laurichesse D, Mercier F, Berthias JP, Broca P, Cerri L (2009) Integer ambiguity resolution on undifferenced GPS phase measurements and its application to PPP and satellite precise orbit determination. Navigation 56(2):135–149. https://doi.org/10.1002/j.2161-4296.2009.tb01750.x
Laurichesse D, Privat A (2015) An open-source PPP client implementation for the CNES PPP-WIZARD demonstrator. In: Proceedings of the ION GNSS+ 2015, September 2015, Tampa, Florida
Laurichesse D, Blot A (2016) Fast PPP convergence using multi-constellation and triple-frequency ambiguity resolution. In: Proceedings of the 29th international technical meeting of the satellite division of the Institute of Navigation (ION GNSS+ 2016), Portland, Oregon, September 2016, pp 2082–2088. https://doi.org/10.33012/2016.14633
Li B, Shen Y (2008) Assessment of stochastic models for GPS measurements with different types of receivers. Chin Sci Bull 53:3219–3225. https://doi.org/10.1007/s11434-008-0293-6
Li P, Zhang X (2014) Integrating GPS and GLONASS to accelerate convergence and initialization times of precise point positioning. GPS Solut 18(3):461–471. https://doi.org/10.1007/s10291-013-0345-5
Li P, Zhang X (2015) Precise point positioning with partial ambiguity fixing. Sensors 15(6):13627–13643. https://doi.org/10.3390/s150613627
Li X, Zhang X, Ge M (2011) Regional reference network augmented precise point positioning for instantaneous ambiguity resolution. J Geodesy 85:151–158. https://doi.org/10.1007/s00190-010-0424-0
Li B, Shen Y, Feng Y et al (2014a) GNSS ambiguity resolution with controllable failure rate for long baseline network RTK. J Geodesy 88:99–112. https://doi.org/10.1007/s00190-013-0670-z
Li B, Verhagen S, Teunissen PJG (2014b) Robustness of GNSS integer ambiguity resolution in the presence of atmospheric biases. GPS Solut 18:283–296. https://doi.org/10.1007/s10291-013-0329-5
Li P, Zhang X, Ren X et al (2016) Generating GPS satellite fractional cycle bias for ambiguity-fixed precise point positioning. GPS Solut 20:771–782. https://doi.org/10.1007/s10291-015-0483-z
Li Z, Chen W, Ruan R et al (2020) Evaluation of PPP-RTK based on BDS-3/BDS-2/GPS observations: a case study in Europe. GPS Solut 24:38. https://doi.org/10.1007/s10291-019-0948-6
Liu G, Lachapelle G (2002) Ionosphere weighted GPS cycle ambiguity resolution. In: Proceedings of the ION national technical meeting, San Diego, CA, USA, 28–30 January 2002, pp 1–5
Liu T, Chen H, Chen Q et al (2021) Characteristics of phase bias from CNES and its application in multi-frequency and multi-GNSS precise point positioning with ambiguity resolution. GPS Solut 25:58. https://doi.org/10.1007/s10291-021-01100-7
Loyer S, Perosanz F, Mercier F, Capdeville H, Marty JC (2012) Zero-difference GPS ambiguity resolution at CNES-CLS IGS analysis center. J Geodesy 86(11):991–1003
Ma H, Zhao Q, Verhagen S, Dl P, Liu X (2020) Assessing the performance of multi-GNSS PPP-RTK in the local area. Remote Sens 12:3343
Matzka J, Bronkalla O, Tornow K, Elger K, Stolle C (2021a) Geomagnetic Kp index. V. 1.0. GFZ Data Services

Matzka J, Stolle C, Yamazaki Y, Bronkalla O, Morschhauser A (2021b) The geomagnetic Kp index and derived indices of geomagnetic activity. Space Weather. https://doi.org/10.1029/2020SW002641
Mervart L, Lukes Z, Rocken C, Iwabuchi T (2008) Precise point positioning with ambiguity resolution in real-time. In: Proceedings of ION GNSS, pp 397–405
Nadarajah N, Khodabandeh A, Wang K, Choudhury M, Teunissen PJG (2018) Multi-GNSS PPP-RTK: from large- to small-scale networks. Sensors 2018(18):1078. https://doi.org/10.3390/s18041078
Odijk D (2000) Weighting ionospheric corrections to improve fast GPS positioning over medium distances. In: Proceeding of the ION GNSS 2000, Institute of Navigation, Alexandria, VA, USA,19–22 September 2000, pp 1113–1123
Odijk TPJG, Zhang B (2012) Single-frequency integer ambiguity resolution enabled GPS precise point positioning. J Surv Eng 138(4):193–202
Petit G, Luzum B (2010) IERS technical note no. 36, IERS conventions 2010, International Earth Rotation and Reference Systems Service, Frankfurt, Germany
Psychas D, Verhagen S (2020) Real-time PPP-RTK performance analysis using ionospheric corrections from multi-scale network configurations. Sensors 20:3012
Saastamoinen J (1972) Atmospheric correction for the troposphere and stratosphere in radio ranging of satellites. In: Henriksen SW, Mancini A, Chovitz BH (eds) The use of artificial satellites for Geodesy, vol 15. Geophysical Monograph Series. AGU, Washington, DC, pp 247–251
Schmid R, Dach R, Collilieux X et al (2016) Absolute IGS antenna phase center model igs08.atx: status and potential improvements. J Geodesy 90:343–364. https://doi.org/10.1007/s00190-015-0876-3
Shi J, Gao Y (2014) A comparison of three PPP integer ambiguity resolution methods. GPS Solut 18(4):519–528
Teunissen PJG (1995) The least-squares ambiguity decorrelation adjustment: a method for fast GPS integer ambiguity estimation. J Geodesy 70(1–2):65–82. https://doi.org/10.1007/BF00863419
Teunissen PJG (1998) Success probability of integer GPS ambiguity rounding and bootstrapping. J Geodesy 72(10):606–612
Teunissen PJG (2005) Integer aperture bootstrapping: a new GNSS ambiguity estimator with controllable fail-rate. J Geodesy 79(6/7):389–397
Teunissen PJG, Khodabandeh A (2015) Review and principles of PPP-RTK methods. J Geodesy 89(3):217–240
Teunissen PJG, Odijk D, Zhang B (2010) PPP-RTK: results of CORS network-based PPP with integer ambiguity resolution. J Aeronaut Astronaut Aviat 42(4):223–229
Verhagen S (2003) On the approximation of the integer least-squares success rate: which lower or upper bound to use. J Glob Position Syst 2(2):117–124
Verhagen S (2005) On the reliability of integer ambiguity resolution. Navigation 52:99–110
Wanninger L (1995) Improved AR by regional differential modeling of the ionosphere. In: Proceedings of the 8th international technical meeting of the satellite division of the US Institute of Navigation, Palm Springs. CA, USA, 12–15 September, 1995, pp 55–62
Wu JT, Wu SC, Hajj GA, Bertiger WI, Lichten SM (1993) Effects of antenna orientation on GPS carrier phase. Manuscr Geodaet 18(2):91–98
Wubbena G, Schimitz M, Bagge A (2005) PPP-RTK: precise point positioning using sate-space representation in RTK networks. In: Proceedings of the 18th international technical meeting of the satellite division, Long Beach, CA, USA, 13–16 September 2005, pp 2584–2594
Xiang Y, Gao Y, Li Y (2020) Reducing convergence time of precise point positioning with ionospheric constraints and receiver differential code bias modeling. J Geodesy 94:8. https://doi.org/10.1007/s00190-019-01334-x
Zhang B, Teunissen PJG, Odijk D (2011) A novel un-differenced PPP-RTK concept. J Navig 64(S1):S180–S191
Zumberge J, Heflin M, Jefferson D, Watkins M, Webb F (1997) Precise point positioning for the efficient and robust analysis of GPS data from large networks. J Geophys Res 102:5005–5017

Publisher's Note